



HAL
open science

A new methodology for predicting fatigue properties of bearing steels: from X-ray micro-tomography and ultrasonic measurements to the bearing lives distribution

Alexandre Stienon, Arnaud Fazekas, Jean-Yves Buffière, Pascal Daguier,
Ferhat Merchi, Alain Vincent

► To cite this version:

Alexandre Stienon, Arnaud Fazekas, Jean-Yves Buffière, Pascal Daguier, Ferhat Merchi, et al.. A new methodology for predicting fatigue properties of bearing steels: from X-ray micro-tomography and ultrasonic measurements to the bearing lives distribution. *Journal of ASTM International (JAI)*, 2010, 7 (3), pp.1-14. 10.1520/JAI102532 . hal-01669982

HAL Id: hal-01669982

<https://hal.science/hal-01669982>

Submitted on 9 May 2023

HAL is a multi-disciplinary open access archive for the deposit and dissemination of scientific research documents, whether they are published or not. The documents may come from teaching and research institutions in France or abroad, or from public or private research centers.

L'archive ouverte pluridisciplinaire **HAL**, est destinée au dépôt et à la diffusion de documents scientifiques de niveau recherche, publiés ou non, émanant des établissements d'enseignement et de recherche français ou étrangers, des laboratoires publics ou privés.



Distributed under a Creative Commons Attribution 4.0 International License

A New Methodology for Predicting Fatigue Properties of Bearing Steels: From X-Ray Micro-Tomography and Ultrasonic Measurements to the Bearing Lives Distribution

Alexandre Stienon,¹ Arnaud Fazekas,² Jean-Yves Buffiere,³ Pascal Daguiet,⁴ Ferhat Merchi,⁵ and Alain Vincent⁶

ABSTRACT: This work aims at developing a new methodology for predicting the distribution of fatigue lives of bearings versus steel microstructure, namely, concentration, morphology, and properties of residual inclusions in steel. On the experimental side, X-ray micro-tomography and high frequency ultrasonic testing are used to provide the required inclusion characteristics. A physically based model is used to compute the number of cycles to crack nucleation and crack propagation up to the surface. For the statistics predictions, the inclusions and/or stringers are distributed randomly in the bearing steel according to the concentration of stringers provided by ultrasonic data. The distributions of the fatigue lives predicted by the model are compared successfully to the experimental distributions determined by fatigue tests performed on flat washer machines. Finally, it is shown that the model is able to predict the influence of the orientation of stringers on the fatigue lives.

KEYWORDS: rolling contact fatigue, bearing steel, inclusions, stringers, distribution of fatigue lives

Introduction

Non-metallic inclusions are known to have a detrimental effect on the fatigue performance of high strength steels, but producing steels with perfect cleanliness is not possible for mass productions at competitive costs. However, international standards, such as ISO 281 [1], do not include explicitly inclusion characteristics in the methods of calculating the basic rating life. Hence, predicting the influence of inclusions on bearing lives remains a major challenge for steel producers, bearing manufacturers, and machine industries. In previous works [2–4], a physically based model for predicting the distribution of bearing lives was developed on the basis of spherical inclusions distributed randomly in the steel. In fact, due to the elaboration process of bearing steels, real inclusions have complex shapes and are often lined up, thus forming so-called stringers. To improve the relevance of such a physically based model, these configurations should be taken into account, especially to be able to describe the influence of the forming process on fatigue properties. This is the topic of the present paper.

For that purpose, a new methodology has been developed. It is based on (i) the determination of the concentrations of detrimental inclusions in the steel by high frequency ultrasonic testing; (ii) the study of the morphologies of single inclusions or stringers by X-ray micro-tomography, which now enables one to obtain three-dimensional (3D) images of inclusions, thanks to the high flux beams of X rays provided by synchrotrons of third generation; (iii) the characterization of the mechanical properties, in terms of elasticity and plasticity, of the inclusions by nano-indentation; and (iv) the random distribution of inclusions

¹ Ph.D., Saint-Gobain, European Research Center (CREE), 550, Avenue Alphonse Jauffret, B P 2 24, 8 4306 C availion CEDEX-France

² Assistant Professor, Université de Lyon, INSA Lyon, Lab. MATEIS, UMR CNRS 5510, Bât. Saint Exupery, 69621 Villeurbanne, France.

³ Professor, Université de Lyon, INSA Lyon, Lab. MATEIS, UMR CNRS 5510, Bât. Saint Exupery, 69621 Villeurbanne, France.

⁴ Research Group Manager, ASCOMETAL CREAS BP 70045, 57301 Hagondange Cedex, France.

⁵ Research Engineer, ASCOMETAL CREAS BP 70045, 57301 Hagondange Cedex, France.

⁶ Professor, Université de Lyon, INSA Lyon, Lab. MATEIS, UMR CNRS 5510, Bât. Saint Exupery, 69621 Villeurbanne, France.

and/or stringers in the bearing steel according to the concentrations provided by ultrasonic data and the computation of the resulting fatigue lives by using a physically based model for crack nucleation and crack propagation up to the surface.

The experimental conditions are described in the first part of the paper. In the second part, some experimental results are illustrated, especially for micro-tomography observations. Then, the modeling conditions are described, and the distributions of fatigue lives predicted by the model are compared to the experimental data derived from fatigue tests performed on flat washer machines. Finally, the influence of the orientation of stringers on the fatigue lives is studied.

Experimental Conditions

Material

The work has been carried out on various heats of 100Cr6 steel, heat treated according to standard conditions: 20 min austenitization at 850°C followed by isothermal quenching at 220°C and 1 h tempering at 170°C. The resulting 0.2 % yield strength is 2360 MPa at room temperature. Additional details about the mechanical properties of the studied material can be found in Ref 2. It should be noted that the studied heats were selected with poor cleanliness according to the purpose of this work.

Ultrasonic Testing

Ultrasonic testing is commonly used to detect and estimate the concentration of non-metallic inclusions in steel. The main advantage of this technique arises from its ability to scan a large volume of material [5]. Details about the technique can be found in dedicated literature [6]. In the present work, this technique has been used for the purposes of (i) estimating the inclusion population in the various heats that have been tested in fatigue and (ii) detecting and locating typical inclusions prior to the X-ray micro-tomography observations. An immersion C-scan Epsilon[®] device from Metalscan,⁷ equipped with an 80 MHz focused transducer, has been used. With this equipment, inclusions of 10 μm in diameter located in the focal zone can be detected. However, the spatial resolution of the technique does not enable one to reveal the detailed shape of inclusions. Such a goal can be reached by using X-ray micro-tomography, as described in the following section.

X-Ray Micro-Tomography

X-ray micro-tomography is a 3D imaging technique that is increasingly used in materials science [7–10]. It allows one to visualize the inner constituents (pores, inclusions, phases, etc.) of a material, provided they exhibit an X-ray absorption coefficient different from that of the matrix. Although several papers dealing with constituent particles in aluminum alloys can be found in the literature (see, for example, Ref 11), to the best of the authors' knowledge, the detailed characterization of inclusions embedded in a high strength steel matrix has not been reported yet.

The examples of observations presented in this work have been obtained on beam line ID19 at the European Synchrotron Radiation Facility (ESRF). This beam line provides an X-ray beam with high brightness and high spatial coherence, allowing one to perform micro-tomography with a spatial resolution in the micrometer range. Figure 1 shows the experimental micro-tomography set-up available at beam line ID19 [12]. It includes a monochromator that allows one to select photons with a suitable energy, a scintillator converting X-rays into visible light, and a digital camera to record the radiographs obtained for successive angular positions of the specimen mounted on a rotating stage. To observe inclusions with the high spatial resolution required for this work, the size of the samples has to be limited. This limitation arises mainly from two factors. First, the size of the specimen affects the choice of the energy of the photons. As a rule of thumb, a minimum of 10 % of the intensity of the incident beam should remain transmitted throughout the specimen to get good quality images, which plays in favor of an increasing energy of the photons with increasing the size of the specimen. But, in contrast, a lower energy tends to be required to keep a good contrast of absorption between inclusions and matrix as well as a good efficiency

⁷Metalscan, Industrial Echography: www.metalscan.fr.

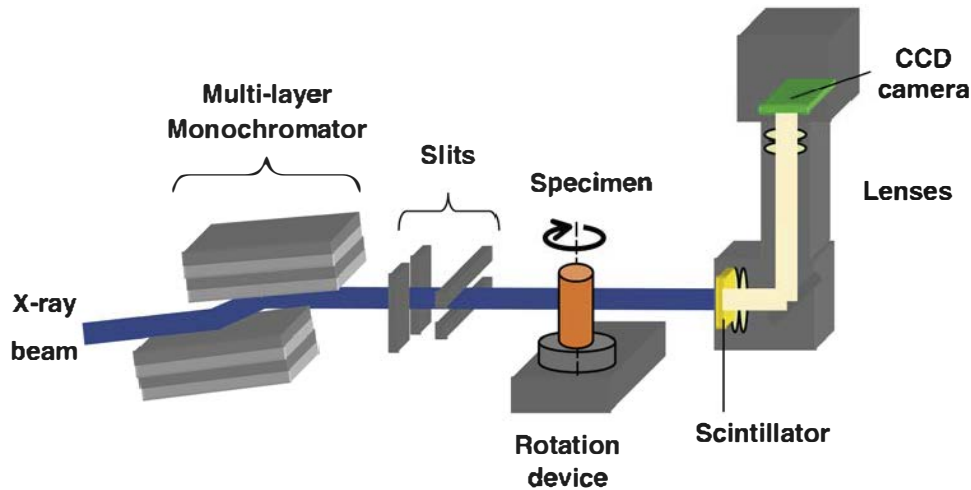


FIG. 1—Experimental set-up available at line ID19 for micro-tomography experiments.

of the scintillator used to detect X-rays. For the present investigations, these conflicting requirements were fulfilled by setting the energy of the incoming photons to 35 keV. Second, the image of the specimen must remain within the field of the charge-coupled device detector of the camera. This depends on the size of the specimen, the optical magnification, and the desired voxel size in the reconstructed image. With the optical magnification chosen, the effective voxel size in the reconstructed 3D image is $0.7 \times 0.7 \times 0.7 \mu\text{m}^3$. Altogether, these conditions inferred a cross section of $0.4 \times 0.4 \text{ mm}^2$ for our needle-like specimens. Once reconstructed by the software available at ESRF (classical filtered back projection method), the 3D images have been analyzed using ImageJ⁸ and Amira⁹ softwares. 3D renditions of the inclusions have been obtained by the region growing segmentation method [13].

Experimental Results

Inclusion Observations through X-Ray Micro-Tomography

The various types of non-metallic inclusions most often met in bearing steels have been observed successfully by X-ray micro-tomography: isolated inclusions with a globular shape, stringers constituted of lined up inclusions, and continuous elongated inclusions. Examples of such observations are shown in Fig. 2 for a few inclusions. The 3D renditions are presented after image processing, which enables one to make the matrix transparent and visualize only the inclusions in a virtual parallelepiped box showing the limits of the volume analyzed around of the inclusion.

Figure 2(a) shows an example of elongated inclusion that appears as a long continuous ribbon (length > 1 mm), with its main direction almost parallel to the axis of the bar from which the specimen was cut. Its section is approximately constant throughout the ribbon, typically $8 \times 20 \mu\text{m}^2$. Furthermore, the inclusion is not perfectly straight but rather undulating around its main direction. It should be emphasized that due to this undulating character, the continuity of such type of inclusion could not be easily evidenced by standard two-dimensional micrographic observations. By means of destructive energy dispersive X-ray analysis, such inclusions have been identified as manganese sulfides in the batches of steels investigated in this work.

Figure 2(b) shows an example of a stringer with lined up inclusions. For a given stringer, the size of the constituent inclusions is widely scattered (from a few microns to $70 \mu\text{m}$ in the case presented in Fig. 2(b)). The distances between neighboring inclusions are also widely scattered and were found to vary from a few microns to a few tens of microns for the investigated samples. It should be pointed out that such detailed characteristics of the stringers could not be obtained by ultrasonic echography. Besides, in such stringers, destructive analyses have shown that the constitutive inclusions are alumina inclusions and calcium aluminate inclusions, sometimes with some coating of calcium enriched sulfide.

⁸ImageJ: <http://rsb.info.nih.gov/ij/>.

⁹Amira: www.amira.com.

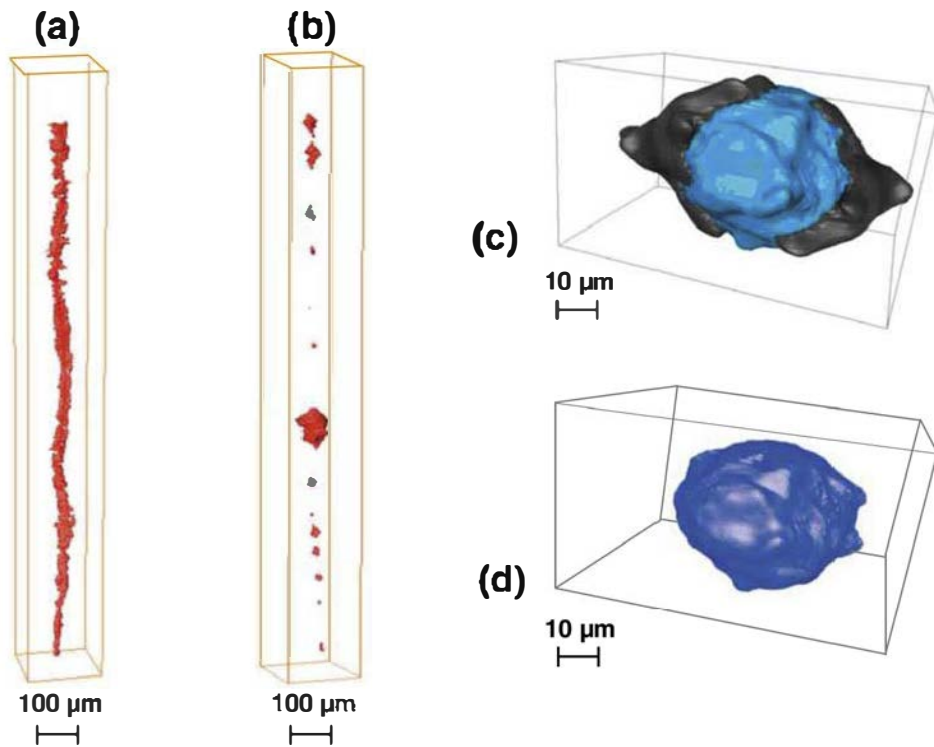


FIG. 2—3D renditions of typical inclusions observed by X-ray micro-tomography in bearing steels: (a) Non-fragmented elongated inclusion; (b) fragmented elongated inclusion; (c) globular inclusion with adjacent conical ends; and (d) same inclusion as (c) but the conical ends have been removed by image processing.

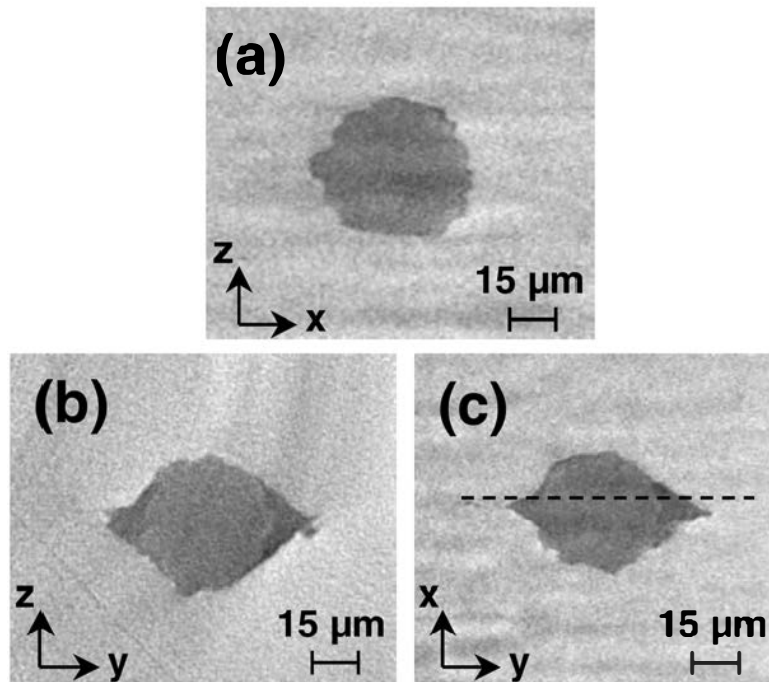


FIG. 3—Reconstructed tomography slices of the globular inclusion shown in Fig. 2(c) observed in three perpendicular median planes. y axis is parallel to the rolling axis of the bar. Two cones appear in darker gray in (b) and (c) on each side of the inclusion. The dotted line in picture (c) corresponds to the observation plane in Fig. 4.

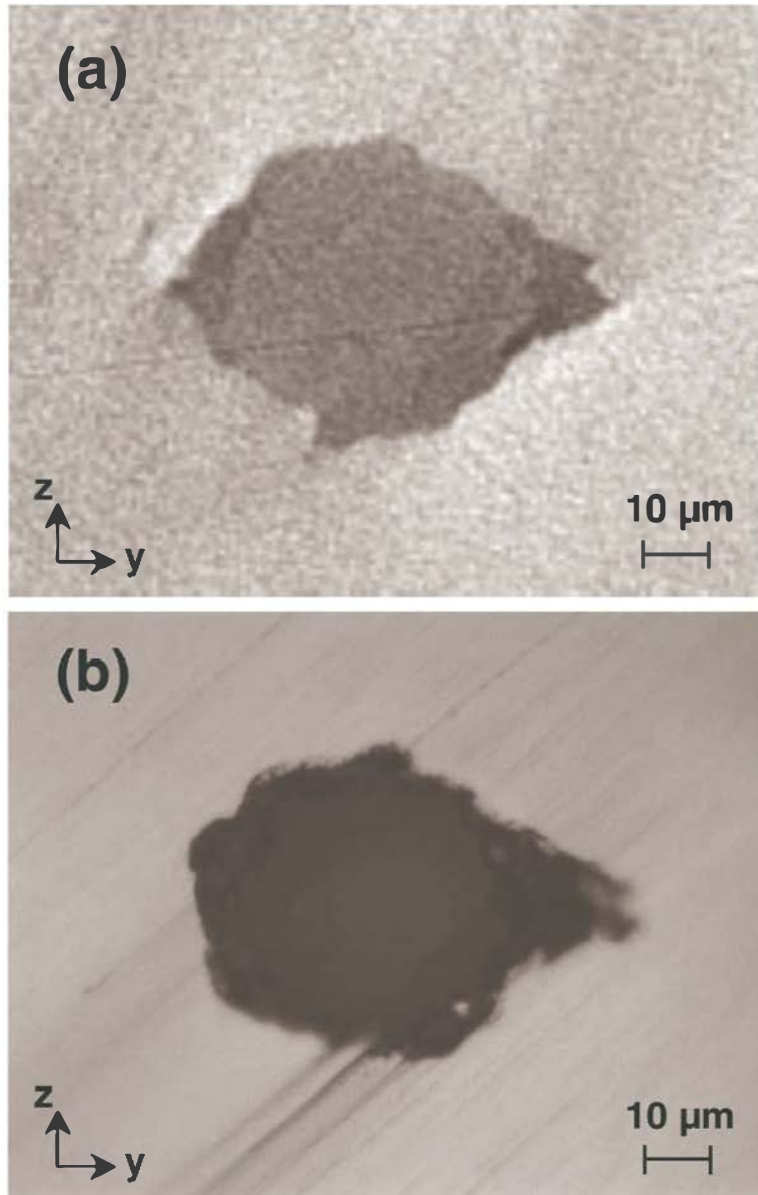


FIG. 4—Comparison between (a) X-ray micro-tomography and (b) optical micrography of the globular inclusion shown in Figs. 2(c) and 3.

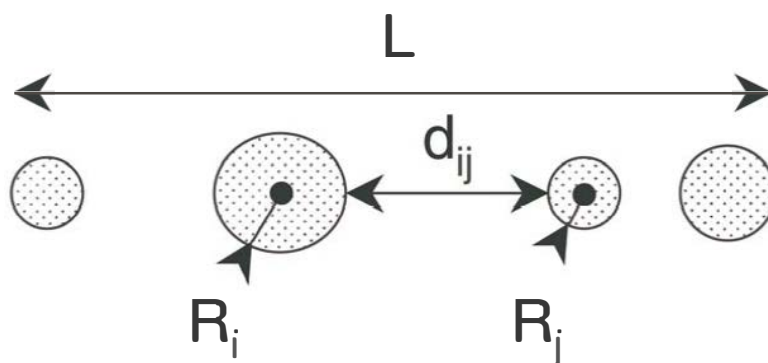


FIG. 5—Schematic of a stringer: Definition of parameters.

Figure 2(c) shows an example of an isolated globular inclusion. It should be mentioned that they often include two conical ends, as the one selected for the figure. The axis going through the two tips of the cones is nearly a revolution axis of the whole defect and is parallel to the rolling direction of the bar. The gray level for these conical ends, darker than those of the steel matrix and the inclusion core, suggests that they are cavities. This contrast can be used to remove the conical ends by image processing (Fig. 2(d)). Such globular isolated inclusions have been identified either to alumina or calcium aluminate inclusions.

The flexibility of the tomography representation is illustrated in Fig. 3. It shows three different virtual tomography cuts of the inclusion shown in Fig. 2(c) in orthogonal median planes. The inclusion is globally spherical but exhibits some surface irregularities. The aforementioned cones are also visible in Fig. 3(b) and 3(c) (darker zone).

Finally, Fig. 4 shows a comparison between a virtual tomography cut and a classical micrograph on a polished section of the same inclusion. This comparison confirms the ability of tomography to depict all the details of inclusions with a spatial resolution close to that of optical microscopy.

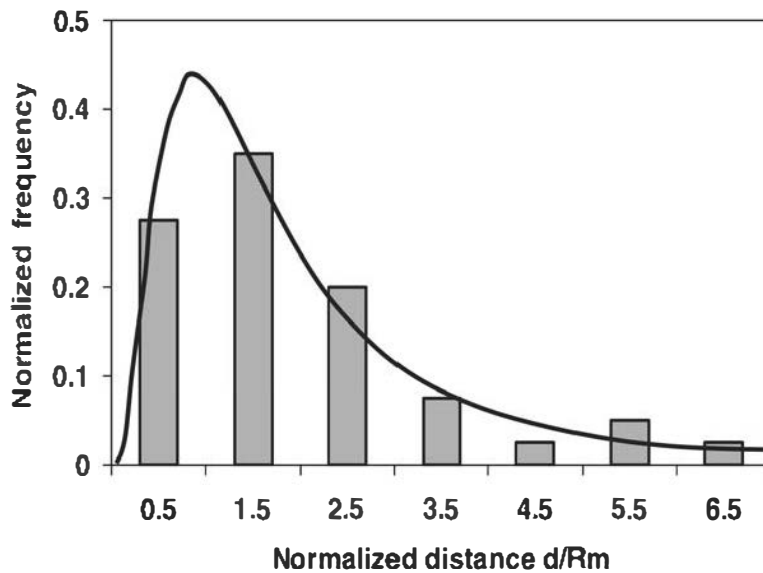


FIG. 6—Histogram of the normalized distances between inclusions in the stringers (for the normalized distance axis, numbers refer to the medium value of each class whose width is 1); the corresponding distribution is fitted by a log-normal function (continuous curve).

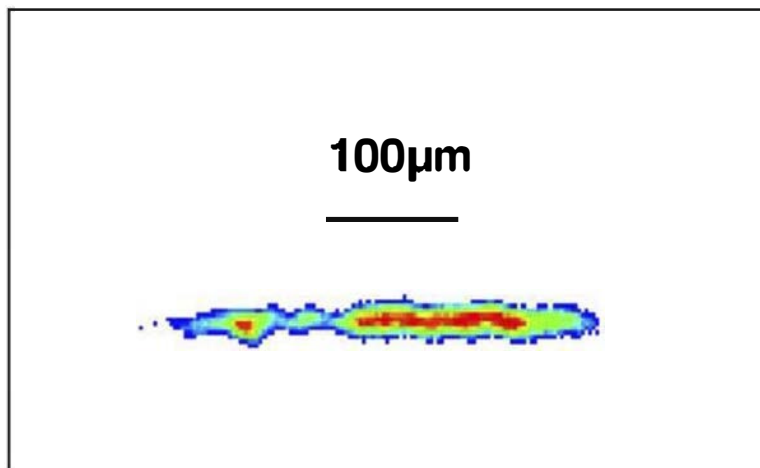


FIG. 7—C-scan image of a stringer detected by high frequency ultrasonic echography.

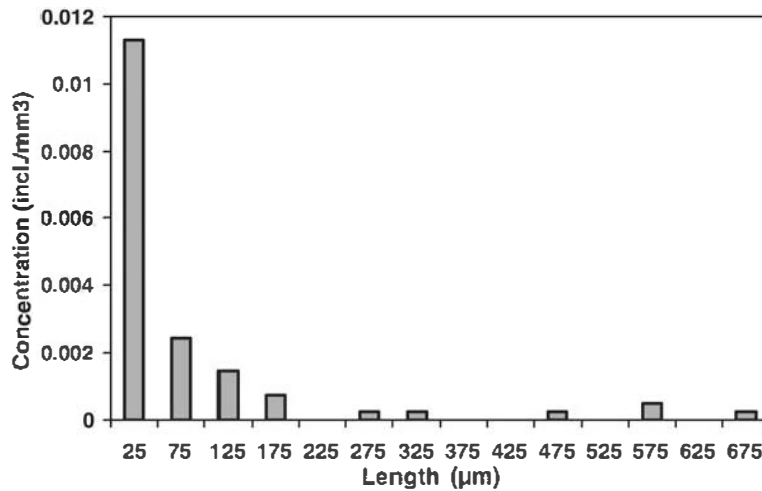


FIG. 8—Histogram of the lengths of the stringers in the heat *D* (for the length axis, numbers refer to the medium value of each class whose width is 50 μm).

Quantitative Characterization of Stringers from X-Ray Micro-Tomography Images

As it will be detailed in the section devoted to modeling, the detrimental character of a stringer is linked to the interaction between constitutive inclusions. This interaction is linked to the distance between neighboring inclusions, which is widely scattered, as mentioned above. Moreover, the size of the interacting inclusions plays also an important role. Hence, the edge-to-edge distance d between two neighboring inclusions has been normalized by the average of the radii of these inclusions $R_m = (R_i + R_j)/2$ (see Fig. 5). In order to characterize this parameter, several 3D images of stringer were analyzed to establish statistical data related to the tested heats. The histogram of the parameter d/R_m thus obtained is given in Fig. 6. It shows that the maximum of the distribution of the normalized distance occurs for d/R_m values close to one. For further use of these data, it can be seen that the distribution can be reasonably fitted by a log-normal distribution (continuous curve in Fig. 6).

Stringer Concentration Obtained through High Frequency Ultrasonic Testing

The stringers can be easily detected by using the ultrasonic equipment referenced in the previous section. For that purpose, parallelepiped samples were taken from the laminated bars, machined, and then scanned with the point focused 80 MHz probe. The scanning plane was parallel to the bar axis. Figure 7 shows an example of a C-scan image thus obtained. As pointed out previously, the resolution of the technique does not enable one to distinguish the details of the stringer. Only its total length L (see Fig. 5) can be estimated. Thus, the ultrasonic testing and the X-ray micro-tomography technique appear quite complementary. Furthermore, for each heat tested in this work, a total volume of about 4 cm³ has been investigated. The stringers have been classified according to their length. An example of histogram of the length of the stringers is shown in Fig. 8. Most of the stringers have a length shorter than 200 μm, but a few were found to belong within categories of longer length.

Finally, it should be mentioned that, up to now, the ultrasonic testing was not able to recognize the nature of inclusions in the detected stringers. Hence, the nature of the inclusions, or at least the majority of them, has to be known using another technique.

Computational Modeling of the Distribution of the Fatigue Lives

The approach used for predicting the distribution of fatigue lives in the present work consists in introducing the effects of interaction of neighboring inclusions in stringers in a model initially designed for isolated spherical inclusions, which has been presented in previous works [2–4]. This is made possible due to both the internal characteristics of the stringers provided by X-ray micro-tomography and the statistical data provided by ultrasonic testing.

The computational modeling of the bearing lives distribution includes two parts. The first one is of

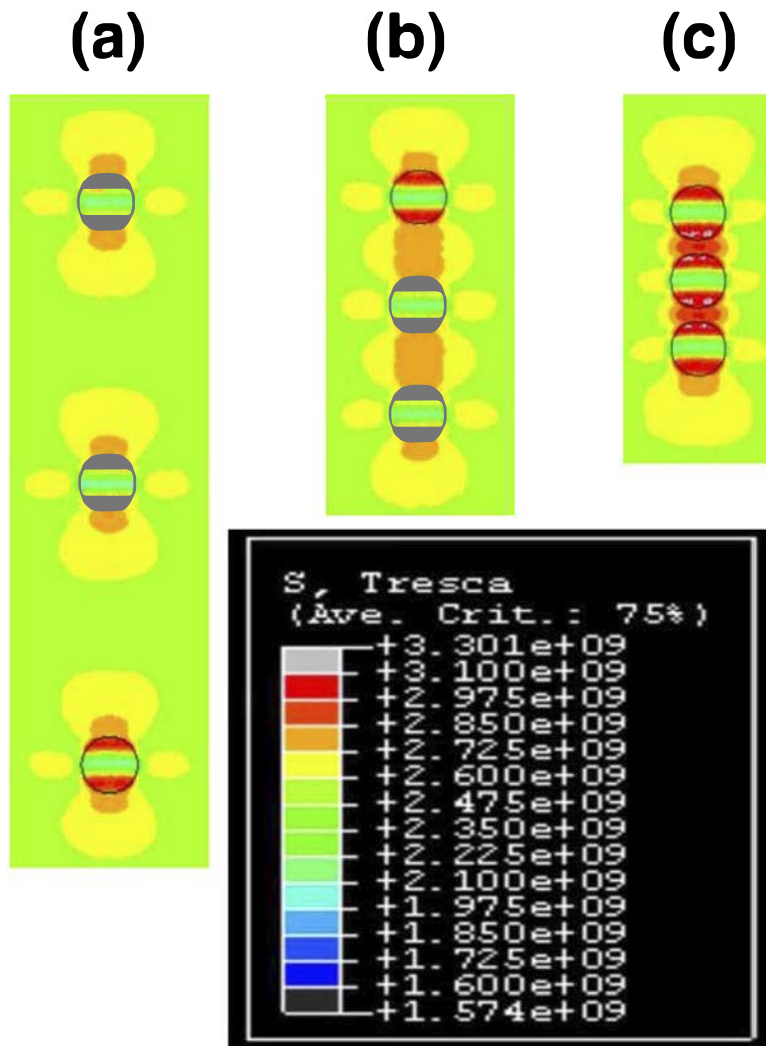


FIG. 9—Tresca stress maps for a stringer oriented perpendicularly to the contact surface for various distances between constitutive inclusions: (a) $d/R_m = 8$; (b) $d/R_m = 2$; (c) $d/R_m = 0.5$; case of alumina inclusions; and applied stress taken at the center of the Hertz field for a Hertz pressure of 4.2 GPa.

determinist nature: It aims at calculating the number of cycles to failure induced by a given inclusion. This problem is solved by considering the crack nucleation and the crack growth stages successively. The second part deals with the statistical aspect of the problem: The inclusions are statistically distributed in the bearing steel (position, size, etc.).

Determinist Model for Crack Nucleation and Growth [2]

The material is loaded cyclically under the repeated contact pressure produced by the rolling bodies. Crack nucleation originating from inclusions arises from the stress concentration around the inclusions. This induces cyclic micro-plasticity leading to the accumulation of dislocations. Finally, crack nucleation occurs once a critical density of dislocations is reached in this area.

In the present work, the contact stress field is that produced by circular balls (9.992 mm in diameter) on a plane surface. The resulting contact stress, 4.2 GPa, is that of the fatigue tests on flat washers described in the last section of the paper. The stress concentration around the inclusions has been computed by means of the Abaqus finite element software, as described in Ref 14. Moreover, in this reference, it has been shown that the real geometry of the inclusions provided by the 3D images from micro-tomography can be reasonably modeled by simplified shapes in order to derive by finite element a realistic stress field around the inclusions (for instance, the inclusion shown in Figs. 2(c) and 3 can be valuably modeled by a spherical core associated with two conical empty sides [14]). The elasto-plastic behavior of the 100Cr6 matrix and the inclusions are also given in this reference. The accumulation of dislocations in

the vicinity of inclusions is characterized by the damage accumulation factor f^* defined in Ref 2, and the criterion for crack nucleation can also be found in Ref 2. The resulting cycle number for crack nucleation is N_n . The orientation of the micro-crack is given by the direction of the maximal shear stress for dislocation glide. Its initial length is taken equal to that of the zone where localized dislocation movements occur, i.e., the stress concentration zone around the inclusion [2].

Crack propagation is calculated by considering a physically based model as in Ref 3. The crack is assumed to grow in mode II with a circular shape. The amplitude of the stress intensity factor for crack growth is calculated by considering an effective shear stress that accounts for friction of the crack lips due to the compression stress normal to the crack plane. To account for the limited extension of the Hertzian loading, the width extension of the crack is bounded to the contact width of the rolling ball. The current crack length, a , is calculated numerically by integrating the local crack growth rate da/dN , which is updated (in relation to the present crack length and the crack position in the loading stress field) after each numerical step. The number of cycles to bearing failure, N_p , is considered necessary for the crack to reach the surface. This means that the number of cycles from the surface breaking stage of the crack to complete spalling is neglected.

Finally the total cycle number to failure, N_R , is given by the sum $N_R = N_n + N_p$.

Influence of the Interaction between Inclusions

In this work, the excess of harmfulness of stringers has been assigned to the interaction between neighboring inclusions, which reduces the number of cycles to crack nucleation N_n . Indeed, the superposition of the stress concentration zones around the neighboring inclusions enhances locally the stress concentration. This mechanism is illustrated in Fig. 9 for a simple stringer made of three spherical inclusions of equal diameter, with the axis of the stringer oriented perpendicularly to the contact surface. Figure 9 shows the Tresca stress maps in a plane passing through the axis of the stringer for different normalized distances d/R_m between the inclusions. It appears clearly that the local stress increases markedly when d/R_m is decreased down to 0.5. It should be pointed out that any local stress increase generally induces a stronger effect on the local cyclic micro-plasticity that governs the damage accumulation. Moreover, it has been shown elsewhere [15] that the number of inclusions in the stringer does not influence significantly the maximal value of the local stress. In other words, for a given inclusion the stress concentration in the surrounding matrix is mainly influenced by the next neighboring inclusion. This fact enables one to characterize the interaction between constitutive inclusions by studying simple stringers made of three inclusions.

Furthermore, a stress enhancement factor has been defined for the stringers by

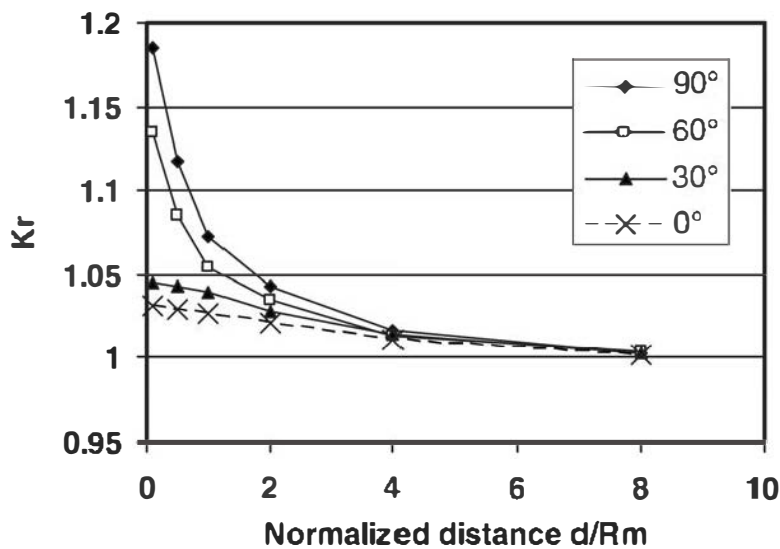


FIG. 10—Stress enhancement factor, K_r , for aluminum stringers as a function of the normalized distance between neighboring inclusions for various orientations of the stringer (0° = parallel to the contact surface; 90° = perpendicular to the contact surface).

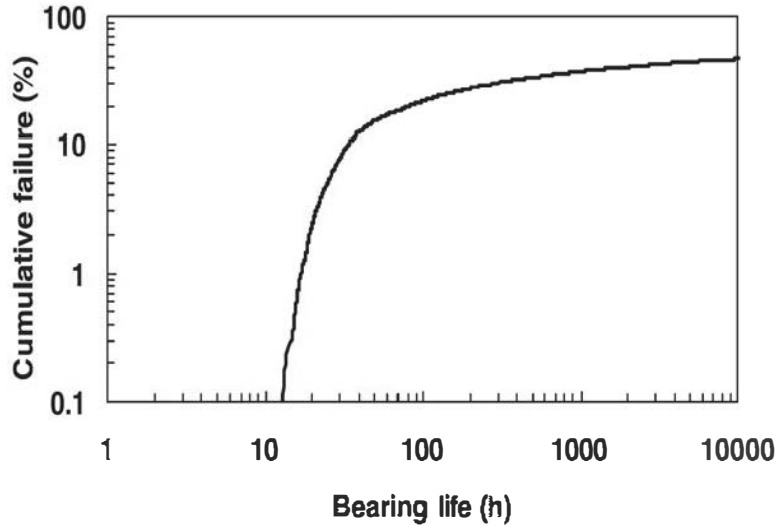


FIG. 11.—Simulated cumulative probability of failure versus life for 10 000 flat washers plotted in a log-log diagram for heat D; 1 h \equiv 675 000 cycles.

$$K_r = \frac{[\sigma_{Tr}^{\max}]_{\text{stringer}}}{[\sigma_{Tr}^{\max}]_{\text{single I}}}$$

where:

$[\sigma_{Tr}^{\max}]_{\text{stringer}}$ and $[\sigma_{Tr}^{\max}]_{\text{single I}}$ = maximal values of the Tresca stress in the steel matrix in presence of interaction between neighboring inclusions and for a single inclusion of the same type, respectively.

The stress enhancement factor, K_r , for alumina stringers has been plotted versus the normalized distance between neighboring inclusions in Fig. 10 for various orientations of the stringer with respect to the contact surface. As already mentioned, the stress enhancement increases steeply as the normalized distance decreases. Moreover, Fig. 10 shows that K_r is also markedly influenced by the orientation of the stringer, the orientation perpendicular to the contact surface (orientation of 90°) being the more detrimental. It is worth mentioning that this stress enhancement factor has to be calculated prior to the statistical calculations described in the following paragraph. Thus, the stress concentrations do not need to be computed again for every particular stringer, but they can be simply derived from a single constitutive inclusion. This method drastically reduces the computation time for the statistical predictions.

Statistical Prediction of the Distribution of Fatigue Lives

The statistical implementation of the model for predicting the distribution of fatigue lives has been carried out in the following way.

- For each considered steel heat, a series of virtual flat washers is built using a Monte Carlo method for drawing successively the number of stringers of a given type in each flat washer, the position of each stringer center (uniform distribution), its total length, and the corresponding d/R_m parameter. It should be specified that the number and the total length of each stringer are drawn according to the experimental distribution determined by ultrasonic echography (see example in Fig. 8), while the d/R_m parameter is drawn according to the distribution determined by X-ray micro-tomography (see Fig. 6).
- Every flat washer is subjected to a virtual fatigue test, and the number of cycles N_F to fatigue failure is computed by applying the models for crack nucleation and growth described above for every stringer in every flat washer; according to the weakest link rule, the fatigue life N_F of a given washer is defined as the minimum value among all the values corresponding to the various stringers; once they are analyzed, all these minimum values form the distribution of lives related both to the heat and the conditions of fatigue testing.

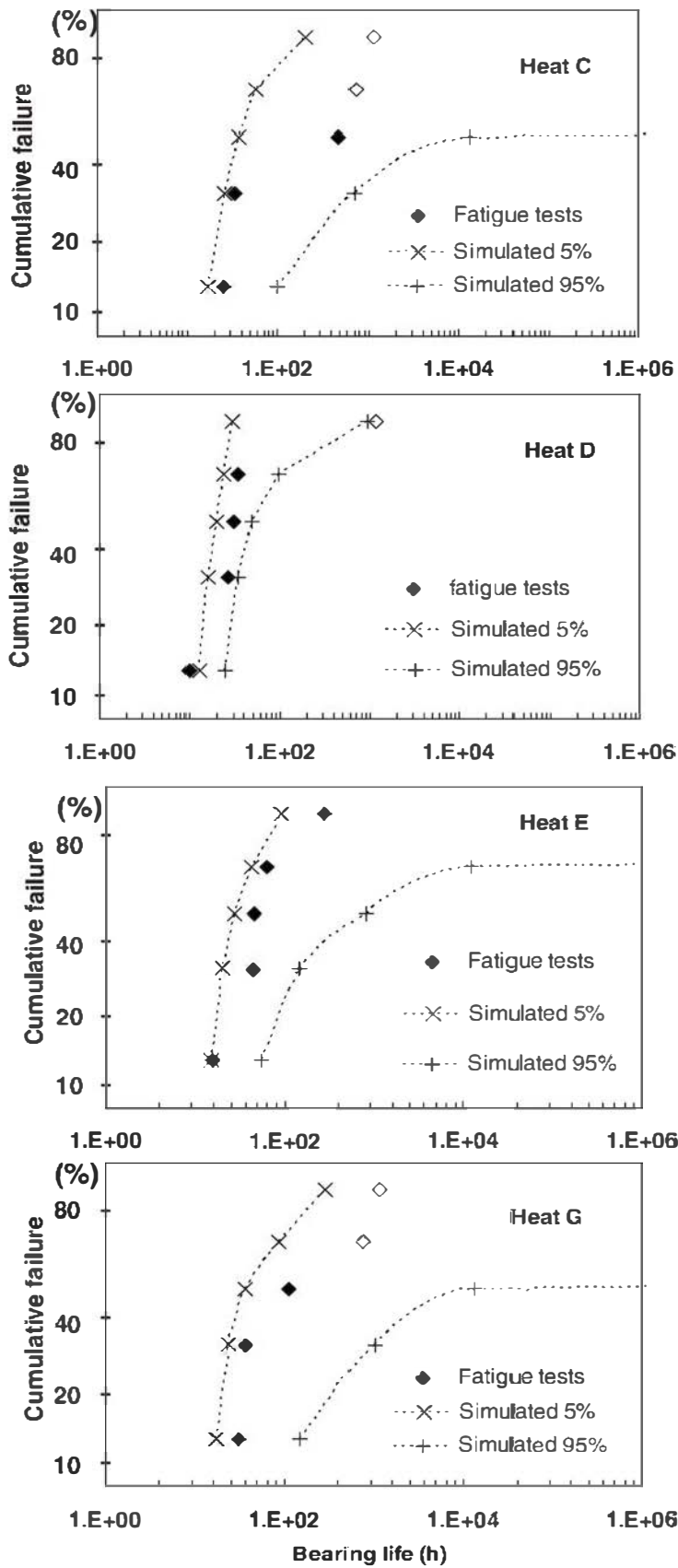


FIG. 12—Comparison between the experimental cumulative probability of failure versus life for sudden death tests plotted in a Weibull diagram and the computed scattering ranges for a confidence interval of 90 %: Examples of heats labeled C, D, E, and G. The open symbols indicate that the corresponding tests were interrupted.

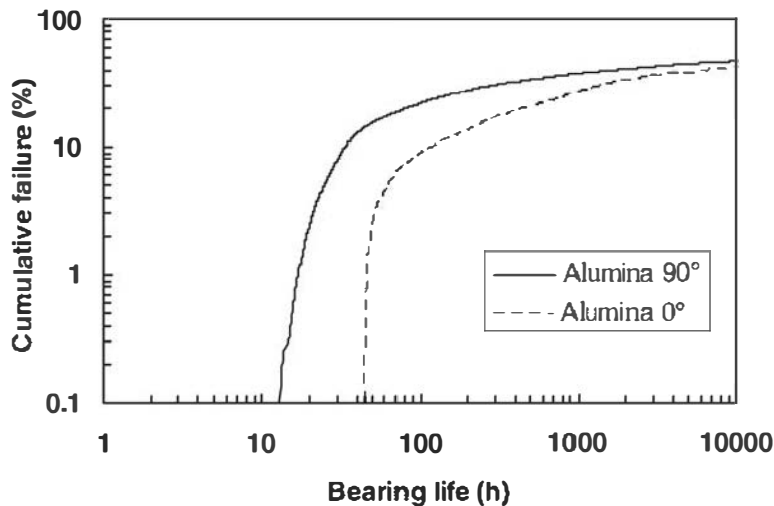


FIG. 13—Comparison between the predicted cumulative probability of failure versus life for stringers oriented parallel or perpendicular to the contact surface (inclusion concentrations are those of heat D).

Application and Comparison with Experimental Data

The assessment of the methodology for predicting the distribution of fatigue lives has to be carried out by comparing the computed fatigue lives to experimental ones. This has been achieved by investigating eight different heats chosen with different cleanliness levels. For that purpose, on the one hand, rolling contact fatigue tests have been carried out on flat washer specimens using SNR Roulements type FB2 test rigs [16]. On the other hand, the cleanliness of every heat has been characterized by ultrasonic testing, as explained previously (see Fig. 8).

The experimental tests were conducted according to the “sudden death testing method” [16]. Thus, 50 washers were tested by groups of five units under a nominal Hertzian pressure of 4.2 GPa. For time reasons, fatigue tests without failure after running 1000 h or so were interrupted.

On the simulation side, for a given heat, first a series of 10 000 virtual washers has been built up and the corresponding lives have been calculated. From experience feedback, the constitutive inclusions in the distributed stringers were assumed to be alumina inclusions in the presented computations. This procedure provides the overall rolling fatigue properties of the heat, which can be presented as the cumulative probability of failure versus life, in a classical logarithmic diagram. Figure 11 shows an example of such a representation for heat D characterized in Fig. 8. As shown in earlier works [3], the overall cumulative distribution of fatigue lives exhibits a typical Γ shape. The tendency of the cumulated failures to saturate well below 100 % is linked with the significant probability to have washers with no detrimental stringers in the core of the Hertzian stress field.

Finally, in order to compare simulations with experimental data, the simulated data have to be analyzed according to the “sudden death” method. Moreover, since a single experimental test exhibits a random character, the scattering range of the results has to be determined. For that purpose, 100 virtual sudden death tests of 50 washers were built up from the 10 000 virtual tests. The cumulative distribution function of each number of failure (Nos. 1–5) can be derived from these results. Then, the scattering range of the results with a confidence interval of 90 % was obtained from these distribution functions. Finally, the five experimental data points and the computed scattering range were plotted in the same Weibull diagram for every heat. Four examples are reported in Fig. 12.

First, it can be seen that the computed scattering ranges are generally wide. As a matter of fact, in Fig. 12 the scattering range appears to be narrower for heat D that is less clean than the other heats. Such a relationship between the scattering width and the inclusion concentration can be explained easily. For a clean heat the probability to find a harmful inclusion in the stressed region below the raceway is low, and hence fatigue failure is a quite random process. In contrast, for a less clean heat the probability to find harmful inclusions in the same region is close to one, thus reducing the randomness of the fatigue process. Second, the experimental data fall well within the computed scattering ranges, except for some interrupted tests (open symbols in Fig. 12). In fact, these results remain consistent with the predicted ranges because an interrupted test potentially refers to a real life longer than the number of cycles to interruption. A similar

agreement was obtained for all the investigated heats. All these good agreements show that the new model presented in this section is able to predict reasonably well the statistical distribution of fatigue lives of bearings in relation with the steel cleanliness characterized by high frequency ultrasonic testing and X-ray micro-tomography. It is worth pointing out that estimating the scattering ranges by means of the experimental fatigue tests would take about 4 years for one heat with seven rigs running continuously. This shows the great advantage of the modeling route.

Finally, regarding the influence of the stringer orientations, Fig. 13 shows the comparison between the distributions of fatigue lives for stringers oriented parallel and perpendicular to the contact surface. It appears that for the perpendicular orientation (90°), the first failures occur significantly earlier than for the parallel orientation (0°). This is mainly due to the higher stress concentration for the perpendicular orientation, which has been shown in Fig. 10. In fact, such a larger stress significantly reduces the number of cycles to crack nucleation, but it does not influence the tendency to saturate as much. This is not surprising because, as mentioned above, the saturation level of cumulated failures is mainly linked to the concentration of stringers, which was the same for both simulations. It should be mentioned that this influence of the orientation is in good agreement with the trend observed experimentally, which exhibits a L_{10} fatigue life about five times longer for washers machined from a bar to obtain the “parallel orientation” of the stringers than for those machined from the same bar to obtain the “perpendicular one.” Unfortunately, for these results, the high frequency ultrasonic characterization of the heat was not available, and hence, the corresponding simulation was not possible.

Conclusion

A new methodology has been developed for predicting the distribution of fatigue lives of bearings from appropriate characteristics of the inclusion population in the steel.

This work has shown that high frequency ultrasonic testing provides reliable data on concentrations of harmful stringers in bearing steels. X-ray micro-tomography has been used for the first time to visualize the 3D shape of inclusions and stringers. This new technique appears to be quite complementary of the high frequency ultrasonic testing. Indeed, it is able to provide the internal details of stringers, but it is limited to small volumes, while in contrast ultrasonic testing enables one to investigate larger volumes of material but without distinguishing internal details of stringers.

The physically based model presented here makes a clear link between the cleanliness of the steel and its fatigue performances. It has been validated by comparing the predicted distribution of lives with a set of fatigue test data carried out according to the sudden death method.

Moreover, this model is able to (i) account for the influence of the stringers orientation with respect to the contact surface, (ii) make predictions of distribution of fatigue lives for large batches of bearings representative of populations of bearings used in industry, and (iii) estimate the scattering of results for fatigue tests performed on reduced numbers of parts.

Furthermore, it should be pointed out that, in its present form, the applicability of the model is limited to operating conditions for which inclusion initiated damage is the controlling process for bearings failure. For instance, this excludes applications with extremely high contact pressures involving bulk metal fatigue or with very clean steels and surfaces indented by pollution of the lubricant.

In the future, this methodology could be used to optimize the forming process of bearing steels. For instance, the reduction ratio of bars or tubes used for manufacturing bearings governs the characteristics of inclusions and particularly of stringers. Using the presented methodology would enable one to predict the fatigue properties of the final product versus the parameters of the forming process.

Acknowledgments

The ASCOMETAL company is gratefully acknowledged for its continuous support. The writers also wish to thank Dr. G. Baudry and Dr. E. Henault for fruitful discussions and encouragements.

- [1] ISO 281, 2007, “Rolling Bearings—Dynamic Load Ratings and Rating Life,” International Standards Organization, Geneva, Switzerland.
- [2] Vincent, A., Lormand, G., Lamagnère, P., Gosset, L., Girodin, D., Dudragne, G., and Fougères, R.,

- “From White Etching Areas Formed Around Inclusions to Crack Nucleation in Bearing Steels Under Rolling Contact Fatigue,” *ASTM STP 1327*, J. J. C. Hoo and W. B. Green, Eds., ASTM International, West Conshohocken, PA, 1998, pp. 109–123.
- [3] Lormand, G., Meynaud, P., Vincent, A., Baudry, G. L., Girodin, D., and Dudragne, G., “From Cleanliness to Rolling Fatigue Life of Bearings—A New Approach,” *ASTM STP 1327*, J. J. C. Hoo and W. B. Green, Eds., ASTM International, West Conshohocken, PA, 1998, pp. 55–69.
- [4] Fougères, R., Lormand, G., Vincent, A., Nelias, D., Dudragne, G., Girodin, D., Baudry, G., and Daguier, P., “A New Physically Based Model for Predicting the Fatigue Life Distribution of Rolling Bearings,” *ASTM STP 1419*, J. M. Beswick, Ed., ASTM International, West Conshohocken, PA, 2002, pp. 197–212.
- [5] Auclair, G. and Daguier, P., “Appropriate Techniques for Internal Cleanliness Assessment,” *ASTM STP 1419*, J. M. Beswick, Ed., ASTM International, West Conshohocken, PA, 2002, pp. 101–112.
- [6] Birks, A. S. and Green, R. E., “Ultrasonic Testing,” *Nondestructive Testing Handbook (American Society for Non-Destructive Testing)*, Vol. 7, P. McIntire, Ed., Ronald Press Co., New York, 1991.
- [7] Buffière, J.-Y., Cloetens, P., Ludwig, W., Maire, E., and Salvo, L., “In Situ X-Ray Tomography Studies of Microstructural Evolution Combined with 3D Modeling,” *MRS Bull.*, Vol. 33, No. 6, 2008, pp. 611–619.
- [8] Kak, A.-C. and Slaney, M., *Principles of Computerized Tomographic Imaging*, IEEE Press, New York, 1988.
- [9] Baruchel, J., Buffière, J.-Y., Maire, E., Merle, P., and Peix, G., *X-Ray Tomography in Material Science*, Hermes Science Publication, Paris, 2000.
- [10] Banhart, J., *Advanced Tomographic Methods in Materials Research and Engineering*, Oxford University Press, Oxford, UK, 2008.
- [11] Maire, E., Grenier, J. C., Daniel, D., Baldacci, A., Klöcker, H., and Bigot, A., “Quantitative 3D Characterization of Intermetallic Phases in an Al–Mg Industrial Alloy by X-Ray Microtomography,” *Scr. Mater.*, Vol. 55, 2006, pp. 123–126.
- [12] Ludwig, W., Buffière, J.-Y., Savelli, S., and Cloetens, P., “Study of the Interaction of a Short Fatigue Crack with Grain Boundaries in a Cast Al Alloy Using X-Ray Microtomography,” *Acta Mater.*, Vol. 51, 2003, pp. 585–598.
- [13] Russ, J. C., *The Image Processing Handbook*, 2nd ed., CRC Press, Boca Raton, FL, 1994, p. 399.
- [14] Stienon, A., Fazekas, A., Buffière, J.-Y., Vincent, A., Daguier, P., and Merchi, F., “A New Methodology Based on X-Ray Micro-Tomography to Estimate Stress Concentrations Around Inclusions in High Strength Steels,” *Mater. Sci. Eng., A*, Vol. 513–515, 2009, pp. 376–383.
- [15] Courbon, J., Lormand, G., Dudragne, G., Daguier, P., and Vincent, A., “Influence of Inclusion Pairs, Clusters and Stringers on the Lower Bound of the Endurance Limit of Bearing Steels,” *Tribol. Int.*, Vol. 36, 2003, pp. 921–928.
- [16] Baudry, G., Duplomb, G., Giroud, G., Bulit, J. H., Girodin, D., and Jacob, G., “Fatigue Properties Evaluation of Bearing Steel Produced by Rotary Continuous Casting,” *Winter Annual Meeting of the American Society of Mechanical Engineers*, ASME, New York, 1991, Vol. 28, pp. 27–39.